

Three-Dimensional Nanostructures for Photonics

By Georg von Freymann,* Alexandra Ledermann, Michael Thiel, Isabelle Staude, Sabine Essig, Kurt Busch, and Martin Wegener

Recent progress in direct laser writing of three-dimensional (3D) polymer nanostructures for photonics is reviewed. This technology has reached a level of maturity at which it can be considered as the 3D analogue of planar electron-beam lithography. Combined with atomic-layer deposition and/or chemical-vapor deposition of dielectrics—the 3D analogues of planar evaporation technologies, the 3D polymer templates can be converted or inverted into 3D high-refractive-index-contrast nanostructures. Examples discussed in this review include positive and inverse 3D silicon-based woodpile photonic crystals possessing complete photonic bandgaps, novel optical resonator designs within these structures, 3D chiral photonic crystals for polarization-state manipulation, and 3D icosahedral photonic quasicrystals. The latter represent a particularly complex 3D nanostructure.

subsequent coating or infilling techniques that are the counterpart of 2D evaporation techniques. These experimental developments are complemented by theoretical developments as architectures for photonic circuitry in three dimensions, e.g., based on 3D complete photonic-bandgap structures, have also become available over recent years. Furthermore, certain functionalities, such as chirality, even necessarily require 3D photonic structures. Other examples are 3D photonic quasicrystals that not only appeal by their aesthetics and mathematical beauty, but also allow the study of fundamental aspects of wave propagation in structures that are neither strictly periodic nor completely random. With the present

review, we intend to convey a flavor for some of these rapid developments towards truly 3D nanostructures for photonics.

1. Introduction

Throughout the last decades, the field of optics and photonics has seen tremendous progress in such diverse areas as optical waveguide architectures, photovoltaic energy conversion, solid-state lighting devices, lasers, and optical sensors. All of these rely on the availability of planar, i.e., 2D lithography technologies that are borrowed from electronics. However, electronics technology is already rapidly developing towards multifunctional-layer systems and the next logical step is going to truly 3D architectures. Regarding optics and photonics, such 3D lithography technology has emerged over recent years in the form of direct laser writing—the 3D counterpart of 2D electron-beam lithography—and

2. Fabrication of 3D Photonic Nanostructures

In the last twenty years, several techniques for the fabrication of 3D photonic nanostructures have been developed (see, e.g., recent review articles^[1–3]). These techniques can be divided into two groups: techniques realizing large-area structures in a parallel fashion and serial techniques providing greater design flexibility at the cost of reduced fabrication speed. Colloidal self-assembly,^[4] holographic laser lithography,^[5] and phase-mask holography^[6,7] belong to the first group. Self-assembly of colloidal particles (e.g., silica or polystyrene spheres) leads to well ordered 3D structures, the optical properties of which are mainly controlled via the size and the shape of the particles. A prominent example is the artificial opal, one of the “workhorses” in the field of photonic crystals. After inversion with high-dielectric-contrast materials such as silicon, even a complete photonic bandgap opens up and the first complete photonic bandgap at near-IR frequencies has been demonstrated along these lines about ten years ago.^[8] While high-quality bulk samples can be fabricated via this approach, a fundamental limitation is the inherent difficulty to introduce well-defined functional defects.^[2,9] This problem is usually overcome by combining colloidal self-assembly with a serial lithographic technique.^[10,11] While colloidal self-assembly is normally limited to face-centered-cubic structures, holographic laser lithography and phase-mask holography allow for a greater variety of structures.^[12,13] Here, the idea is to create 3D interference patterns, which are used to expose a photosensitive material. After development, a 3D structure remains. The main theoretical

[*] Dr. G. von Freymann, A. Ledermann, Prof. K. Busch, Prof. M. Wegener
Institut für Nanotechnologie
Karlsruhe Institute of Technology
76021 Karlsruhe (Germany)
E-mail: freymann@int.fzk.de

Dr. G. von Freymann, A. Ledermann, S. Essig, Prof. K. Busch,
Prof. M. Wegener
DFG–Center for Functional Nanostructures (CFN)
Karlsruhe Institute of Technology
Wolfgang-Gaede-Straße 1, 76131 Karlsruhe (Germany)

Dr. G. von Freymann, A. Ledermann, M. Thiel, I. Staude
Prof. M. Wegener
Institut für Angewandte Physik
Karlsruhe Institute of Technology
Wolfgang-Gaede-Straße 1, 76131 Karlsruhe (Germany)

S. Essig, Prof. K. Busch
Institut für Theoretische Festkörperphysik
Karlsruhe Institute of Technology
Wolfgang-Gaede-Straße 1, 76131 Karlsruhe, (Germany)

DOI: 10.1002/adfm.200901838



Georg von Freymann received his Ph.D. degree from the Physics Department, Universität Karlsruhe (TH), Karlsruhe, Germany, in 2001. He was a postdoctoral researcher at Institute of Nanotechnology, Forschungszentrum Karlsruhe, Karlsruhe, Germany in 2002 and at the University of Toronto, Toronto, Canada, until 2004. Since 2005 he has been the head of a Junior Research Group in the Emmy Noether-programme of the Deutsche Forschungsgemeinschaft (DFG) at the Institute of Nanotechnology, Forschungszentrum Karlsruhe, Germany. His research interests include near-field microscopy and spectroscopy, nanofabrication technologies, photonic crystals, photonic quasicrystals, and 3D photonic metamaterials. He has been a member of the DFG–Center for Functional Nanostructures (CFN) since 2005 and of the Karlsruhe School of Optics & Photonics (KSOP) since 2006.



Kurt Busch received his Ph.D. degree from the Physics Department of Universität Karlsruhe (TH), Karlsruhe, Germany, in 1996. He was a postdoctoral researcher at the University of Toronto from 1997 to 1999 and head of a Junior Research Group within the Emmy-Noether Programme of the Deutsche Forschungsgemeinschaft (DFG) at Institut für Theorie der Kondensierten Materie at Universität Karlsruhe (TH) from 2000 to 2003. In 2004 he joined the University of Central Florida, Orlando, FL, USA, as an associate professor with a joint appointment between the Department of Physics and the College of Optics & Photonics: CREOL & FPCE. Since 2005 he has been a professor at Institut für Theoretische Festkörperphysik at Universität Karlsruhe (TH). He has been a member of the DFG–Center for Functional Nanostructures (CFN) since 2001 and of the Karlsruhe School of Optics & Photonics (KSOP) since 2006. His research interests lie in the areas of computational photonics and the theory of light propagation and light-matter interaction in strongly scattering systems. This research has led to the Carl Zeiss Research Award of 2006.



After completing his Ph.D. in physics in 1987 at Johann Wolfgang Goethe-Universität Frankfurt, Germany, **Martin Wegener** spent two years as a postdoctoral researcher at AT&T Bell Laboratories in Holmdel, USA. From 1990 to 1995, he was C3-Professor at Universität Dortmund, Germany; since 1995 he has been a C4-Professor at Universität Karlsruhe (TH). Since 2001 he has had a joint appointment at Institut für Nanotechnologie of Forschungszentrum Karlsruhe GmbH. Since 2001 he has also been the coordinator of the DFG–Center for Functional Nanostructures (CFN) in Karlsruhe. His research interests comprise ultrafast optics, (extreme) nonlinear optics, near-field optics, photonic crystals, and photonic metamaterials. This research has led to various awards and honors, among which are the Alfried Krupp von Bohlen und Halbach Research Award 1993, the Baden-Württemberg Teaching Award 1998, the DFG Gottfried Wilhelm Leibniz Award 2000, the European Union René Descartes Prize 2005, the Baden-Württemberg Research Award 2005, and the Carl Zeiss Research Award 2006. He is a member of Leopoldina, the German Academy of Sciences (since 2008), Fellow of the Optical Society of America (since 2008), Fellow of the Hector Foundation (since 2008), and Adjunct Professor at the Optical Sciences Center, Tucson, USA (since 2009).

difficulty is to choose the right set of parameters for the different beams,^[14,15] especially, if a complete photonic bandgap shall eventually be achieved. These parameters can be controlled via the amplitudes and polarizations of the individual beams and the angles between the different beams that are used to create the interference pattern. For holographic laser lithography, this can be directly experimentally implemented. However, these experiments are challenging and not all combinations of parameters are experimentally accessible,^[16] although some progress has been recently reported.^[17,18] In the case of phase-mask holography, a 2- or 3D mask creates the required beams with desired properties out of a single laser beam.^[7,19] Here, the main difficulty lies in calculating the proper phase-mask design and in its fabrication. Despite the greater variety of structures accessible with holographic techniques, they do share some of the drawbacks of the

colloidal self-assembly methods: Most of the structures are fabricated in low-dielectric contrast materials and, hence, do not possess a complete photonic bandgap. While this can, in principle, be overcome via coating and/or infilling techniques (see below), the introduction of functional defects is again inherently difficult. Only very few theoretical designs exist for functional defects inside these holographically created structures^[20] and experimental results for structures with a complete photonic bandgap are, to the best of our knowledge, absent to date.

For some of these holographically created bulk structures, it is known that they open a complete photonic bandgap if they are infiltrated by or replicated into high-dielectric-contrast materials.^[14,15] As most of the polymeric photoresists do not withstand the conditions required for the deposition of high-dielectric-contrast semiconductors, several groups devised procedures to

invert^[21,22] or double-invert^[23] the polymeric templates. Although there are some papers published reporting successful infiltration of holographically fabricated samples with high-dielectric-constant materials,^[7,25] none of them demonstrated a full photonic bandgap to the best of our knowledge. This is most likely due to some inherent topological problems hampering a complete infiltration in gas-phase-based techniques.^[26,27] In total, there are extremely few papers demonstrating the successful inclusion of functional defects (i.e., defects in a complete photonic bandgap) in structures fabricated with one of these parallel techniques.^[11]

The second group of techniques comprises direct-semiconductor or layer-by-layer fabrication^[28–32] and direct writing techniques like direct ink writing^[33] and direct laser writing.^[34,35]

Photonic crystals of extremely high quality have been fabricated using a layer-by-layer approach: semiconductor wafers are two-dimensionally structured with e-beam lithography to yield one layer of the desired structure. Several layers are then stacked on top of each other using micromanipulation techniques^[32] or they are optically aligned and subsequently connected via wafer fusion layer-by-layer.^[30] As the 2D structure of each layer is defined via electron-beam lithography, functional defects such as waveguides or resonators can easily be designed and included into the structure. Even defect layers containing optically active material could be demonstrated along these lines.^[36] However, although in principle any structure could be fabricated in a layer-by-layer fashion if only the layers are thin enough, experimental limitations have so far restricted the use of this technique to the woodpile photonic crystal, Ref. 31 being the exception. Since several technologically challenging steps have to be combined here, the fabrication of samples along these lines is both extremely expensive and very time consuming. The main advantage of this technique is the direct fabrication into high-dielectric-contrast materials. The direct writing techniques sacrifice this advantage for increased fabrication speed and improved structural design freedom.

Direct ink writing fabricates structures by pressing an ink through a nozzle with a cross-section directly defining the cross-section of the smallest possible building block. For example, quadratic cross-sections are preferably used for the fabrication of woodpile photonic crystals. The ink directly solidifies on exiting the nozzle and, hence, allows for the fabrication of almost arbitrary 3D structures.^[33] Nevertheless, the structures cannot be of high complexity as the nozzle has to be able to reach all positions. Crossing already written parts of the structure is impossible. This limitation is absent for direct laser writing.^[37–39] Here, pulses from an ultrafast laser are focused into a photosensitive material in such a way that the intensity reached in the very focal volume is sufficiently high to polymerize the material via two- or multiphoton absorption although the material is completely transparent for the fundamental wavelength of the laser. In principle, almost arbitrarily small features can be generated along these lines. In real world applications two limiting factors appear: i) the laser sources are not perfectly stable, hence, working directly at the two-photon-absorption threshold is almost impossible, and ii) common photoresist materials do not possess an ideally sharp threshold and, furthermore, do not allow for resolution better than the average size of the building blocks. Local inhomogeneities of the monomer/photoinitiator mixture further reduce the achievable resolution, which, however, lies on the order of 80 nm for state-of-

the-art systems. Scanning the sample relative to the focus allows for the fabrication of arbitrarily complex structures. Even multiple crossings of already written structures pose no challenge, provided that a photoresist is used, which does not significantly change its index of refraction during writing. For instance, the commercially available negative-tone photoresist SU-8 fulfills the above requirements. Subsequently, the written structures are developed. Several groups worldwide have established their own direct laser writing setup.^[34] To the best of our knowledge, the greatest variety of different 3D photonic crystal structures has been fabricated using this technique: woodpile,^[40] slanted-pore,^[41] square,^[42] and round-spiral photonic crystals^[43]—with and without functional defects, chiral photonic crystals,^[44,45] and photonic quasicrystals.^[46] Most of the photosensitive materials that can be structured with direct laser writing do not possess sufficiently high dielectric contrast to realize a complete photonic bandgap. Some of us have recently introduced a photoresist system based on the chalcogenide glass arsenic-trisulfide (As₂S₃) and a specially developed etchant. This photoresist system overcomes the low dielectric contrast^[47,48] and also allows for the spatially selective inclusion of optical active material via doping with erbium.^[49] However, most of the times the polymeric photoresist structures are used as templates for the inversion or double-inversion into high-dielectric-contrast materials such as semiconductors^[2,21–26] or metals.^[50,51] Hence, structures fabricated using direct laser writing are at the focus of this article, demonstrating very interesting avenues for functionality besides the original schemes relying on complete photonic bandgaps. High-dielectric-contrast structures can boost the observed effects, but they are not mandatory.

3. Functional Defects in 3D Photonic Crystals

Functional defects in 3D photonic crystals—in contrast to 2D structures—potentially allow for the integration of functional elements in several layers of the photonic crystal and, hence, for dense 3D optical circuitry. Theoretical blueprints for such dense integration of certain functional optical elements in three dimensions exist for some years now. Most of these designs are based on the woodpile photonic crystals, although some designs have been proposed for inverse opal and square spiral structures^[52] as well. Here, we want to demonstrate that an approach based on direct laser writing (DLW) and templating is suitable for the fabrication of these structures. First of all, it is of crucial importance to check whether the quality of the fabricated templates is sufficient to guarantee the existence of a complete photonic bandgap after conversion into a high-dielectric-contrast structure. In this light, it is well known that polymer templates shrink during the development process and several countermeasures have been devised.^[40,53,54] Thus, we start by reviewing the optical properties of the (face-centered-cubic) woodpile photonic crystal template. Templates are fabricated using DLW (for details, see Experimental section) in the negative-tone photoresist SU-8 with the following parameters: rod distance $a = 1.0 \mu\text{m}$, 24 layers, footprint $100 \mu\text{m} \times 100 \mu\text{m}$. The templates are surrounded by a massive rectangular wall to reduce the effects of strain due to photoresist shrinkage.^[40,55] After development, angle-resolved transmittance measurements are performed using

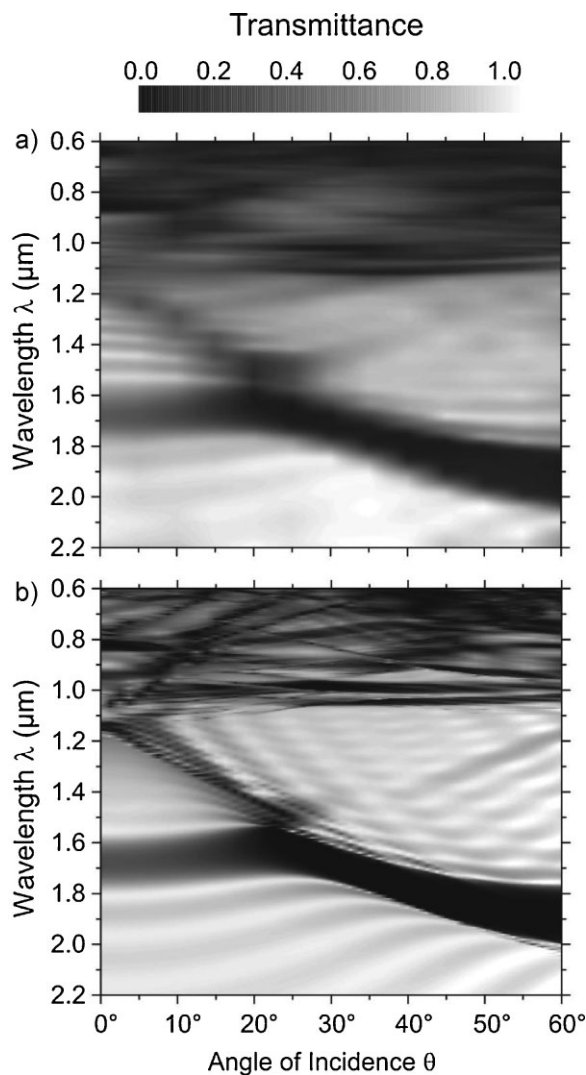


Figure 1. Angular resolved transmittance spectra of a woodpile photonic crystal. a) Experimental data and b) numerical calculation. Reproduced with permission from [55]. Copyright 2005 American Institute of Physics.

a home-built white-light microspectrometer setup.^[55] Figure 1a depicts the experimental data. The most prominent feature is the fundamental stopband, located around $1.65 \mu\text{m}$ wavelength under normal incidence. This stopband shifts slightly to the red for oblique incidence. Starting at wavelengths around $1.1 \mu\text{m}$ and below, the clear signature of higher photonic bands is visible, a very good indicator of high sample quality. How close are these templates to ideal structures? To address this question, we calculate the expected optical properties with a home-made scattering-matrix code (for details, see Theoretical section). As input parameters we take the structural data obtained from the template via scanning electron microscopy (SEM) images from top-view images and from focused-ion-beam (FIB) cross-sections. Furthermore, the ellipsoidal shape of the voxels is taken into account. SU-8 photoresist has a real refractive index of $n = 1.57$, its surface roughness is neglected. Calculated transmittance data are referenced identical to the experimental procedure, i.e., to the

transmittance of the bare glass substrate. Along these lines all adjustable parameters have been fixed and detailed, and quantitative comparisons become available. The calculated angle-resolved transmittance of this ideal structure is depicted in Figure 1b. The qualitative agreement with the experiment is excellent. The position, as well as the angular dispersion of the fundamental stopband, is nicely reproduced; the higher bands start at the same wavelength and the Fabry–Pérot fringes due to the finite thickness of the sample are also reproduced. The overall seemingly higher spectral resolution of the ideal structure, especially in the region of the higher bands, is due to the perfect normal incidence in the numerical calculations. In the experiment, data are averaged over the 5° half-opening angle; hence, sharp spectral features tend to smear out.

After silicon-double (single) inversion, a complete photonic bandgap of 8%^[26] (12%^[23]) gap-to-midgap ratio opens up—sufficiently large for the inclusion of functional defects.

One straightforward approach to include functional defects is to combine the design rules worked out for 2D photonic crystals with the advantage of a complete photonic bandgap so as to prevent losses into the third dimension. This has led to so-called 3D–2D–3D photonic crystal heterostructures^[52,56–58] in which a 2D photonic crystal layer (comprising waveguides etc.) is clad by 3D photonic bandgap materials from above and below (for an illustration, see Fig. 2). In principle, losses into the third dimension are eliminated for frequencies inside the 3D photonic bandgap of the cladding material. Furthermore, the vast knowledge on proper circuitry design in 2D photonic crystals can directly be transferred to this case. This concept presents its full power, if not only one, but several functional layers can be densely packed and interconnected in the third dimension.^[59] What kind of changes to the optical properties of the bulk material do we expect by the inclusion of a 2D defect layer? Here, we review our experimental approach^[61] to address this question with two different sets of samples. First, we add the 2D photonic crystal on top of the bulk woodpile photonic crystal (see Fig. 2a), so that inspection with an electron scanning microscope is possible. Second, we realize the full photonic crystal heterostructure, i.e., the 2D photonic crystal is clad between two woodpiles. This structure is then optically characterized, again with angle-resolved transmittance spectroscopy.

Figure 2b–d show SEM images of the 3D–2D heterostructure. The bottom 3D photonic crystal is a woodpile with rod spacing $a = 1 \mu\text{m}$, lattice constant $c = 2^{1/2}a$, 16 layers, and a $80 \mu\text{m} \times 80 \mu\text{m}$ area. The height of the 2D photonic crystal is 150 nm . The posts of the 2D photonic crystal are precisely positioned on top of the intersections of the rods of the underlying woodpile photonic crystal. The two close-ups in Figure 2b demonstrate the precise positioning and the highly reproducible shape of the posts. Functional defects are introduced by omitting one or several rows of these posts. This is demonstrated in Figure 2c, as well as in Figure 2d, where a 90° angle was introduced into the waveguide. Note that omitting one row of posts does not lead to any sample deformation in the vicinity of the defect. The waveguide architectures shown here are not optimized or optically functional, but rather aim at a proof-of-principle. The total writing time for the structure shown in Figure 2 is about 20 min.

The optical properties of this 3D–2D–3D heterostructure are depicted in Figure 3. First of all, it is clear that for incidence of light

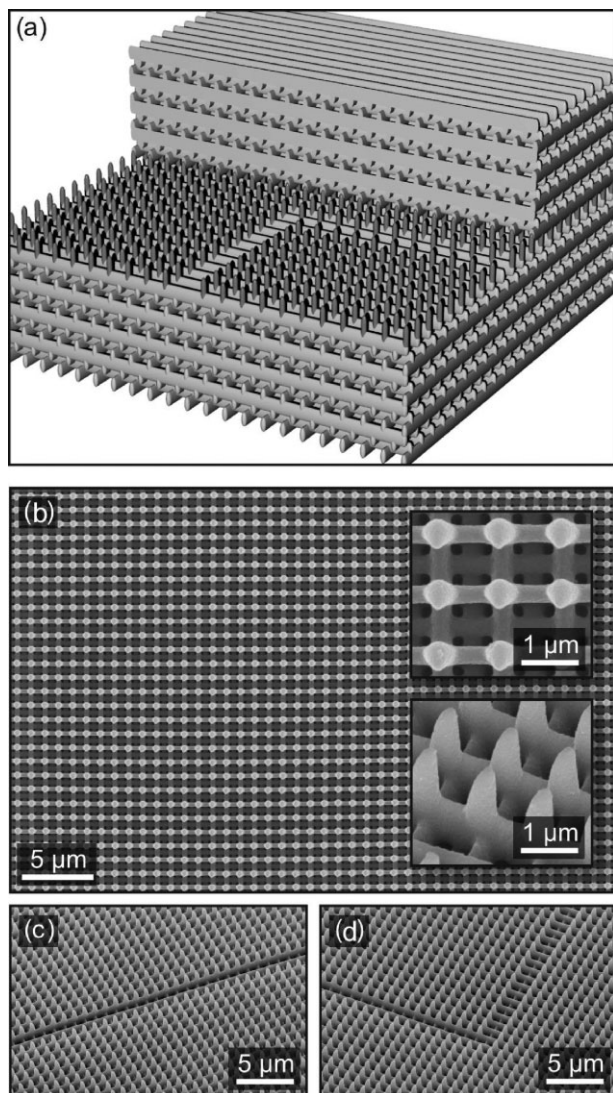


Figure 2. 3D–2D–3D photonic crystal heterostructure: a) schematic of the sample and b) top view SEM image. The two insets are a magnified top view and an oblique incidence view. c,d) Oblique incidence view on a waveguide without and with 90° bend. Reproduced with permission from [60]. Copyright 2006 Optical Society of America.

normal to the 2D plane, the overall structure forms just a Fabry–Pérot cavity. Therefore, we would expect for a proper design to find a transmission mode located in the center of the fundamental stopband. Figure 3a shows angle-resolved experimental transmittance data. The overall optical properties are qualitatively the same as found for the woodpile photonic crystal (compare, e.g., the angle dispersion of the fundamental stopband, the higher bands, and the Fabry–Pérot fringes). Due to a slightly higher filling fraction, the spectra are red-shifted compared to the bulk structure. In addition, we find one new mode located inside the fundamental stopband (see the dotted ellipse), that results from the 2D photonic crystal. In Figure 3b the comparison to an ideal structure is shown. The calculations are exactly the same as described above, but we additionally average over several angles of incidence, mimicking

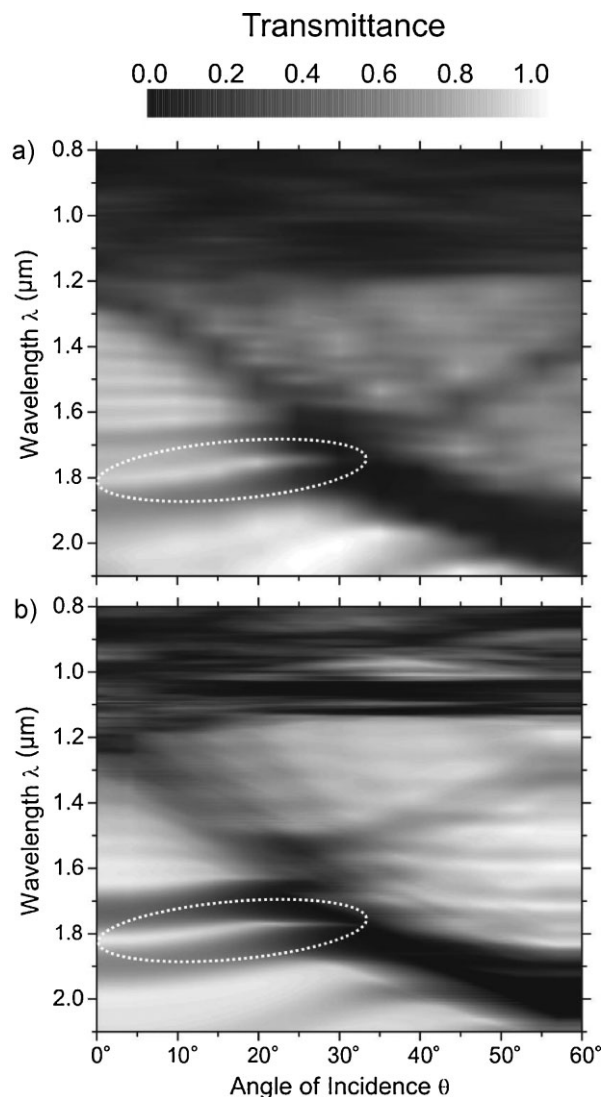


Figure 3. Angular resolved transmittance spectra of a 3D–2D–3D photonic crystal heterostructure. a) Experimental data and b) numerical calculation. The dotted ellipses are guides for the eyes to highlight the additional transmittance mode. Compare with Fig. 1. Reproduced with permission from [60]. Copyright 2006 Optical Society of America.

the finite opening angle of the experiment. Now, as expected, all sharp spectral features are smeared out, especially in the higher bands, resulting in almost quantitative agreement between experiment and calculation. Location and dispersion of the defect mode are also close to the experimentally measured ones. Therefore, the quality of these DLW fabricated templates would again be sufficient for transferring the structures into silicon.

The 3D–2D–3D photonic crystal heterostructures are one access route to denser integration. Why not design circuitry directly for 3D materials without the detour via 2D structures? In 2D photonic crystals simple resonators are created by altering just one elementary cell of the periodic structure. Here, we follow the same idea, but in three dimensions. As the woodpile photonic

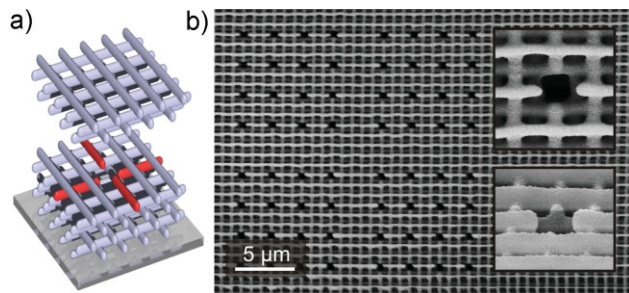


Figure 4. a) Scheme of the 3D resonator design. b) Top-view SEM image of a woodpile photonic crystal containing several defects in its top-most layers. The insets are magnified views of a single defect.

crystal is constructed from a two-rod motif, we actually leave out exactly one of these building blocks, as depicted in Figure 4a. Here, two bars (marked in red) are discontinued symmetrically to their former intersection, forming a resonator with roughly one unit cell in size. Again, we fabricate two sets of samples. One set with the two defect layers on top for scanning electron microscope inspection and another one with the defects buried deep inside, in order to demonstrate that conversion into silicon is actually possible for such complicated structures. Figure 4b depicts a top view of the defect layer. Four fields with 16 defects each are clearly visible. Here, slight variations of the defect parameters are performed exploring the optimum fabrication parameters. The two close ups demonstrate the high fidelity of the defect design. The intersection of the rods is nicely centered, and no obvious bending of the surrounding structure is visible. Sample parameters are a rod spacing of $a = 900$ nm and a length of the intersection of $d = 900$ nm. Figure 5a depicts a sketch of the 3D structure after silicon double-inversion. The obvious voids inside the rods stem from the silicon chemical-vapor-deposition process. This sketch of an ideal structure comes actually very close to the experimental realization, as shown in Figure 5b. Here, a FIB cross-section of a single cavity in a silicon double-inverted structure is shown, which demonstrates the feasibility of our fabrication approach.

To investigate this cavity, we performed scattering-matrix calculations for a similar woodpile structure ($a = 1 \mu\text{m}$, diameter of the rods $w = 0.25 \mu\text{m}$, intersection length $d = 1 \mu\text{m}$, effective index of refraction of the rod material $n = 3.43$ (silicon), rod aspect-ratio = 2). Since the scattering-matrix methodology (see Theoretical section) requires periodicity in the lateral direction, we employed a supercell calculation where a single cavity is located in an array of 5×5 conventional unit cells of the woodpile structure. This ensures that the defect modes of the array are sufficiently decoupled so that both defect frequency and the corresponding mode profile are almost identical with that of an individual defect. Our calculations reveal that this resonator mode is twofold degenerate, as has been expected from the two-rod motif of the woodpile photonic crystal. Figure 5c shows a calculated mode-profile for incident linear polarization parallel to the x -axis and a structure with an overall thickness of 22 layers, whereas the defect is situated in layers 11 and 12. The modulus of the field amplitude is shown in a z -plane at the center of the defect between layers 11 and 12.

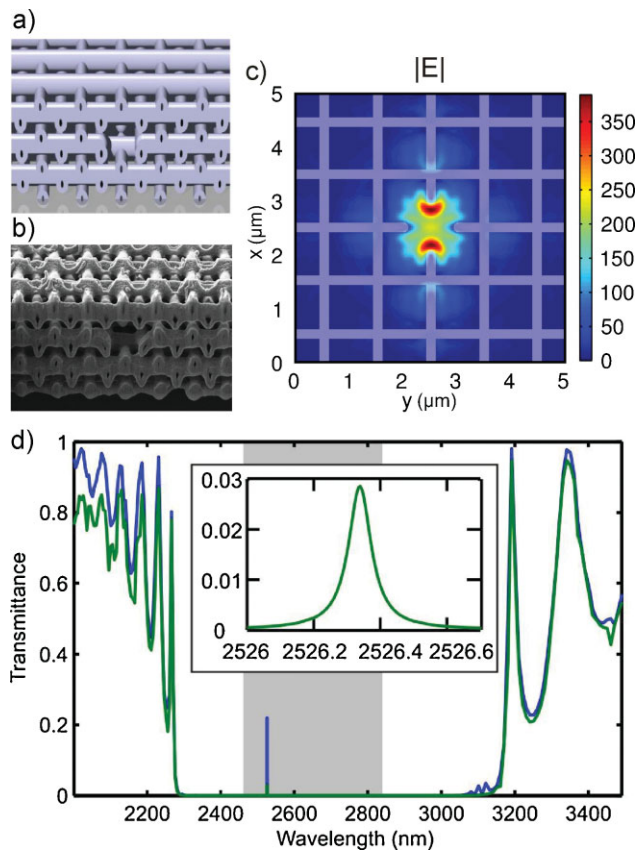


Figure 5. a) Schematic representation of the resonator design after silicon double-inversion. b) FIB cross-section of a silicon photonic crystal with defect. c) Numerical calculation of the mode profile. The grey structure represents the distribution of the silicon and acts as a guide for the eyes. d) Perpendicular incidence transmittance spectra into the forward direction (entire-half space) of a structure containing one resonator, green (blue) solid curve. The inset is a close-up of the transmittance into the forward direction. The grey area displays the width of the complete photonic bandgap.

The second mode can be excited with an incoming polarization parallel to the y -axis, and the resulting field distribution will be oriented along the y -axis. On resonance, the field enhancements is roughly a factor of 350 (corresponding to an intensity enhancement of 122 500), and this illustrates the potential of cavity modes in high-quality 3D photonic crystals with complete photonic bandgaps. The calculated quality factor of this defect is $Q = 30\,000$ and can be further increased by increasing the amount of cladding layers. In theory, one can even reach infinitely large quality factors for infinitely extended samples, in sharp contrast to 2D photonic crystals, where the quality factor stays finite (albeit large). Calculated transmittance spectra for this defect mode in the supercell setting are shown in Figure 5d. The fundamental stopband around 2700 nm wavelength is clearly visible. The complete photonic bandgap (14.3% gap-to-midgap ratio) is marked by the grey shaded area and has been obtained from an independent bandstructure calculation (not shown). The twofold degenerate defect mode is located at 2526.34 nm. The curves depict the transmittance for perpendicular incidence into the forward

direction (green solid line) and into the entire half-space (blue solid line). The close-up allows for a determination of the quality factor for the transmittance in forward direction. Furthermore, the bandstructure calculation reveals a third defect mode inside the complete photonic bandgap that cannot be seen in the transmittance calculations due to a symmetry mismatch between plane-wave excitation and mode profile under perpendicular incidence.

To wrap up this section, we have demonstrated the feasibility of our fabrication approach. Our novel resonator design is perfectly compatible with DLW and subsequent double-inversion steps, and results in an air-type defect. This is an important point, as dielectric defects cannot be reliably fabricated due to the nature of the chemical-vapor-deposition process. In the near future, some efforts are still required to push the complete photonic bandgap into the technologically interesting telecommunication region around 1.5 μm . This latter task is challenging because woodpile photonic crystals with 600 nm rod distance are required. Here, the development of novel photoresists specially designed for 3D nanostructures might bring the breakthrough, as SU-8 has already been pushed to its limits. Regarding theory, promising avenues such as the photonic Wannier-function approach^[61,62] adapted for 3D structures will allow for designing optical circuitry at acceptable computational cost.

Besides these classical photonic crystals, there are many interesting other structures not requiring high-dielectric-index contrast to show novel optical properties or even functionalities. Two examples will be given in the following sections.

4. Chiral Photonic Crystals

Large complete photonic bandgaps have been predicted for high-index contrast silicon square-spiral structures^[63] and corresponding experiments using glancing-incidence deposition,^[64,65] interference lithography,^[66] or direct laser writing^[43,67] have already been published. In addition to complete gaps and stopbands, theory^[68] predicts polarization stopbands, i.e., stopbands for one of the two circular polarizations. These polarization stopbands can give rise to strong circular dichroism,^[65,69,70] which can potentially be used for constructing polarization sensitive devices or even compact “thin-film” optical diodes.^[71] Inspired by cholesteric liquid crystals, chiral layer-by-layer photonic crystals show such polarization behavior.^[72] Here, we want to discuss slightly different structures, namely cork-screw or spiral uniaxial photonic crystals (more precisely, helical photonic crystals) as well as more isotropic bi-chiral photonic crystals.

4.1. Uniaxial Chiral Photonic Crystals

For circular polarization of light, the tip of the electric-field vector follows a spiral. We thus expect a chiral resonance and, hence, strong circular dichroism from spiral photonic crystals if the pitch of circularly polarized light matches the pitch of the dielectric spirals, i.e., the lattice constant a_z . Theory^[68] for high-index silicon-based structures confirms this intuitive reasoning. However, our own scattering-matrix calculations also reveal the same trend, even for low-index-contrast polymeric structures.^[44] The parameters of

the 3D spiral photonic crystals in the following discussion are the result of an optimization with respect to circular dichroism. Again, the structures are fabricated via DLW in SU-8. As free-standing spirals with high aspect ratios tend to fall over (during the development process), all following structures are mechanically supported by a 2D network of bars at or close to the top of the 3D crystal. Furthermore, all structures for optical experiments are again surrounded by a thick massive wall (see Fig. 6a). Here, we use a round wall (rather than a rectangular one as above) in order to evenly distribute strain inside the wall. The inset in Figure 6a shows a close-up cross-sectional view of the sample, from which the following parameters are extracted: in-plane lattice constant $a_{xy} = 1.3 \mu\text{m}$, pitch $a_z = 1.3 \mu\text{m}$, spiral diameter $d = 0.78 \mu\text{m}$, 34.7% volume filling fraction, lateral diameter of the spiral arms $d_{\text{arm}} = 380 \text{ nm}$, ratio between axial and lateral diameter = 2.7, and $N = 8$ lattice constants along the z -direction. As lattice constant and pitch are equal, the structure forms a 3D photonic crystal with a cubic cell. The FIB cross-section furthermore reveals that the spirals are indeed open and not touching each other. To better visualize the top grid, Figure 6b shows spirals with different parameters ($a_{xy} = 1.5 \mu\text{m}$, $a_z = 1.5 \mu\text{m}$, and $N = 4$), stabilized by a similar grid. In the following, we want to discuss only left-handed spirals. Results obtained for right-handed structures show essentially a complementary behavior and can be found elsewhere.^[44]

For the measurements, we extend our home-built white-light setup: the incident polarization state of light is controlled via a combination of a Glan–Thomson polarizer and a super-achromatic quarter-wave plate. This setup gives us access to the spectral range from 500 to 2200 nm wavelength of light.

Figure 6c shows measured transmittance spectra of 3D spiral photonic crystals with identical parameters as those shown in Figure 6a, for normally incident left circular and right circularly polarized light. As expected from our intuitive reasoning,

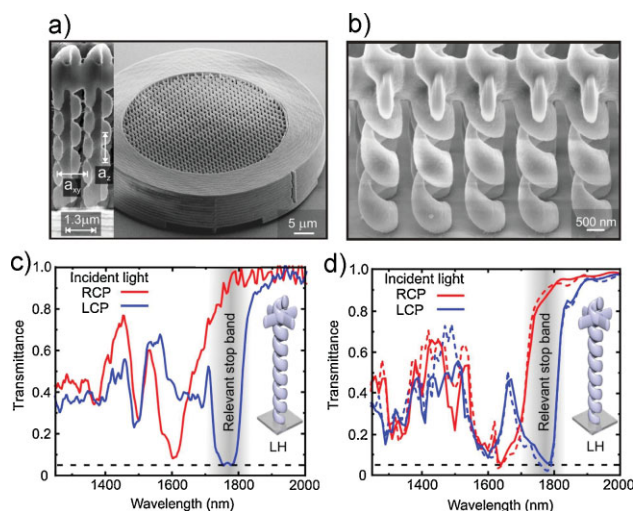


Figure 6. a) SEM images of a spiral photonic crystal. The inset shows a FIB cross-section of the structure and allows for retrieval of the structural parameters. b) Another structure highlighting the stabilizing cross grid. Transmittance spectra for a left-handed structure: c) experimental data and d) numerical calculation. The dashed curves in d are calculated for a structure without the stabilizing top-grid. Reproduced with permission from [44]. Copyright 2007 Wiley-VCH.

propagation of light with matching polarization (blue curve) (i.e., left circular polarization and left-handed spirals) is strongly inhibited for a certain bandwidth, while the other circular polarization (red curve) is transmitted. In the polarization stopband around the 1.8- μm wavelength, the transmittance in the “low state” is around 5% compared to about 95% in the “high state,” corresponding to a ratio approaching twenty.

Figure 6d depicts the corresponding calculated transmittance. Again, we employ our scattering-matrix approach. The geometrical parameters are the same as in the experiment, and we also account for the ellipsoidal shape of the voxels to faithfully reproduce the proper filling fraction of the sample. The refractive indices used for SU-8 and the glass substrate are $n_{\text{SU-8}} = 1.57$ and $n_{\text{glass}} = 1.52$, respectively. We account for the finite opening angle of the focused incident light in the experiment; the calculated transmittance spectra are averaged over a half-opening angle of 5° with respect to the normal. Note again the overall very good agreement between experiment and theory: The symmetry, the spectral position of the polarization stopband, and the depth of the transmittance minima are reproduced very well. Quantitative deviations between experiment and theory at wavelengths at the shorter wavelength-side of the polarization stopband, where many different photonic bands contribute, are likely due to slight sample imperfections. Moreover, one should be aware that the angle-averaging also influences the detailed shape of the spectra, and it is difficult to find the proper weight of all contributing angles. The solid lines in Figure 6d correspond to the full structure of the experiment. The dashed lines are calculated for a structure without the stabilizing grid, hence demonstrating again that the stabilizing grid does indeed not introduce any circular dichroism.

Compared to the circular dichroism observed for chiral layer-by-layer photonic crystals,^[72] we find a rather distinct behavior. While in the case of chiral layer-by-layer photonic crystals the matching polarization is strongly suppressed in the fundamental polarization stopband, but recovers to nearly the same transmittance values for shorter or longer wavelengths, we observe here a behavior on the short wavelength side dominated by diffraction into higher orders and hence no recovery back to nearly 100% transmittance. What is even more striking is the behavior of the nonmatching polarization. While in the case of chiral layer-by-layer photonic crystals this polarization does not experience any change whatsoever around the position of the fundamental polarization stopband, we observe basically the same spectral dependence as for the matching polarization, but blue-shifted by roughly 200 nm in wavelength. This behavior can be explained as follows:^[44] if the pitch of the light spiral inside the structure (i.e., the material wavelength) roughly matches the pitch of the dielectric spiral (i.e., lattice constant a_z), the light field peaks inside the dielectric spiral for both senses of rotation, similar to the behavior of light at the lower dielectric edge of a photonic bandgap (dielectric mode). While the fundamental stopband in a photonic crystal appears at a wavelength roughly twice the lattice constant, we find here the resonance at wavelengths matching the spiral pitch; hence, we operate in the second Brillouin zone. However, for the matching sense of rotation, the light field is more strongly confined to the dielectric, resulting in a higher effective index, and hence, in a longer vacuum wavelength of light for the polarization stopband. Therefore, one observes a polarization stopband for each of the two

circular polarizations (compare Fig. 6c and d). Obviously, the short-wavelength polarization stopband is not attractive for applications because the transmittance in the opposite circular polarization does not come close to unity.

In contrast to chiral layer-by-layer structures, spiral architectures offer the unique opportunity to align the spirals not only along one principal axis, but along all three dimensions. Along these lines one could create a material, which might show a complete polarization stopband for one circular polarization while being perfectly transparent for the other one. Following this idea leads to so-called bi-chiral photonic crystals.

4.2. Bi-chiral Photonic Crystals

The architecture of the bi-chiral photonic crystals that we have recently proposed and realized for the first time^[45] is inspired by so-called blue-phase cholesteric liquid crystals.^[73–75] Our structures consist of left- or right-handed circular dielectric spirals arranged along the three orthogonal axes of a cubic lattice. There are two ways to arrange three orthogonal spirals in space, one with a left- and one with a right-handed so-called corner. Therefore, a total of four possible combinations are available. Nature provides in the blue-phase system only those with opposite handedness, i.e., left-handed motifs on right-handed corners and vice versa.^[76] As there are two types of chirality combined in one structure, we refer to them as “bi-chiral.” The advantage of direct laser written structures is that we are now able to realize all four different combinations and to tune the optical properties over a broad range by adjusting the size of the structures.

The construction principle of our bi-chiral photonic crystals is further illustrated in Figure 7. By displacing the fictitious axes of the spirals by their radius as shown on the right-hand side of Figure 7a, a connection point of the three spirals in the center of each cubic cell can be enforced. After displacing two of the three axes, one is left with two non-equivalent options for positioning the third axis. This choice introduces a second type of chirality to the overall structure that is distinct from the chirality of the spirals. It is clear, by construction, that the chiral optical properties will be identical for propagation of light along the three cubic axes—in sharp contrast to a uniaxial structure.

Figure 7b displays the four possible combinations of the two chiralities. The nomenclature for the following discussion will address a combination of right-handed spirals with a left-handed corner as right/left; the three other combinations are similarly addressed.

The complete bi-chiral photonic crystal is depicted in Figure 7c. The right/right structure consists of three right-handed spirals oriented along the x -axis (red spiral), along the y -axis (blue spiral), and along the z -axis (green spiral). All spiral pitches are equal to maintain the cubic cell that we have already discussed for the uniaxial structure. Before addressing the optical properties of these structures, we should understand the optical properties of the respective building blocks. From the last section, it is clear that a single spiral will show strong circular dichroism for light propagating along the spiral's axis. Nevertheless, a true chiral object shows chirality regardless from which direction it is looked at. Hence, a right-handed spiral should interact differently with left- or right-circular polarized light even under propagation

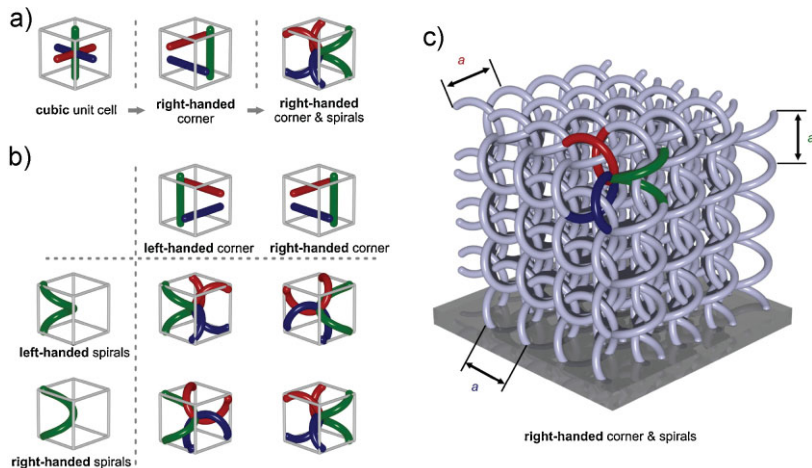


Figure 7. Bi-chiral photonic crystals simultaneously exhibit two distinct types of chirality. The first type stems from the handedness of the circular spirals that are arranged on a simple-cubic 3D lattice. a) Displacing the central spiral axes by half the spiral diameter enforces a mechanical connection point of the three spirals in the center of the unit cell. The orientation of these three fictitious spiral axes (the “corner”) introduces a second type of chirality. b) Combined with the chirality of the spirals, four distinct types of bi-chiral photonic crystals result, i.e., left/left, right/right, left/right, and right/left-handed structures. c) Complete structure. The color coding is the same as in a and b, and serves as a guide for the eye. Reproduced with permission from [45]. Copyright 2009 Wiley-VCH.

perpendicular to its obvious axis. This behavior is demonstrated in the numerical calculations shown in Figure 8. In contrast to Figure 6, we plot here the difference in transmittance between left- and right-circular polarized light (LCP and RCP, respectively). A difference of +1 in this plot means that only LCP light is transmitted; zero corresponds to equal transmittance of LCP and RCP light; and -1 difference indicates 100% transmittance of the RCP light and 0% for LCP. The insets in all parts of the figures display the configuration under study; the light is impinging along the z -axis. In Figure 8a a similar case is displayed as already shown in Figure 6. We find a polarization stopband around $4.75 \mu\text{m}$ —RCP light is reflected back from the right-handed spiral and LCP light is nicely transmitted. The parameters of the spiral are as follows: elliptical cross-section as in the experiment, a lattice constant and pitch of $4 \mu\text{m}$, a spiral diameter of $0.9a$, and the index of refraction of SU-8 $n = 1.57$. If we now calculate the response for the same spiral under perpendicular incidence towards its axis, we still keep strong circular dichroism, although slightly shifted to shorter wavelength (see Fig. 8b). This shift can also be understood along the lines of our above reasoning: here, neither the “matching” nor the “nonmatching” circular polarization can actually follow the spiral; nevertheless, the electric field of RCP light is still more confined to the dielectric structure, resulting in the observed circular dichroism. Combining two spirals as shown in Figure 8c increases the overall filling fraction of the structure and, hence, the effective refractive index. As a result, the polarization stopband shifts towards longer wavelength. The combination of all three spirals finally results in a very pronounced stopband around $5.1 \mu\text{m}$ wavelength (see Fig. 8d). This computed behavior is also found experimentally. Figure 9a shows an electron microscopy image of a right/right structure and Figure 9b the corresponding measurement, plotted in the same way as in

Figure 8. So far, the behavior under perpendicular incidence does not look too different from that of the uniaxial structures. However, the bi-chiral photonic crystal should provide a certain isotropy regarding its chiral properties as this structure shows essentially the same optical properties along each of the three principal axes.

To test this hypothesis, we calculated angle-resolved transmittance spectra for a bi-chiral photonic crystal made from silicon. LCP (RCP) light is impinging under 45° with respect to the z -axis, and the azimuthal angle is rotated from 0° to 360° . The resulting LCP–RCP transmittance is shown in Figure 10. Blue (yellow) areas correspond to high transmittance of LCP (RCP) light. Around $2.5 \mu\text{m}$ wavelength an almost flat polarization stopband is observed. However, one should be cautious in drawing conclusions regarding complete polarization bandgaps on the basis of these data. Note, that we have calculated the optical response for a finite structure with real surfaces. Light impinging under an angle will be refracted at the photonic crystal interface. At this point, its polarization state generally changes. Hence, one cannot necessarily conclude that the dispersion observed in the numerical calculation is connected with real

anisotropy (or isotropy), but might also stem from the different coupling of the incoming light to the modes of the photonic crystal.

Although bi-chiral photonic crystals are truly complex 3D structures, they still rely on periodicity. The optical properties can be numerically predicted in a straightforward manner. In the next section we discuss 3D quasiperiodic structures.

5. 3D Photonic Quasicrystals

Quasicrystals^[77–81] are a class of structures that do not have translational symmetry, but obey local rotational symmetry, very often with symmetry axes forbidden for regular crystals, e.g., five-fold rotational symmetry. Originally discovered for rapidly annealed metallic alloys by Shechtman,^[77] photonic quasicrystals are man-made structures. As quasicrystals combine both, long-range order as in photonic crystals (although not in a repeating fashion) and local arrangements of atoms in fixed positions but with different configuration of the surrounding atoms like in glasses, they promise to possess unusual optical transport properties. While 2D photonic quasicrystals have been studied for several years,^[82–84] 3D photonic quasicrystals for near-infrared frequencies were recently introduced by some of us.^[46] Again, fabrication with DLW is advantageous, as the positions of the fictitious atoms can be precisely controlled. Nevertheless, other groups started fabrication of photonic quasicrystals by means of holographic laser lithography^[85,86] and phase-mask holography.^[87,88] How can one determine the positions of the fictitious atoms? Quasicrystals can be generated by projection of a higher-dimensional rotated ordinary crystal into three dimensions. This mathematical procedure is known as the cut-and-project method.^[80] As this method only delivers the positions of the

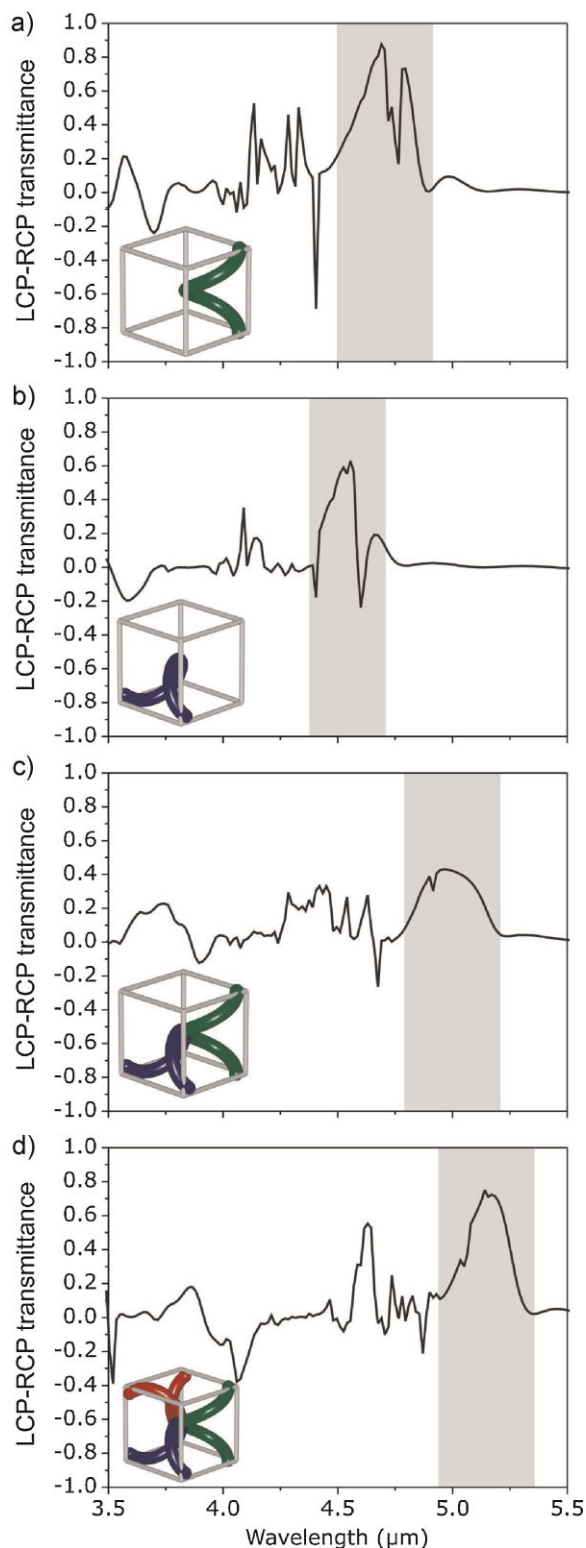


Figure 8. Numerical calculations: LCP–RCP transmittance of structures which are eight unit cells high and infinitely extended in the xy -plane. The corresponding unit cell is shown as an inset in a–d. Color coding is the same as in Fig. 7.

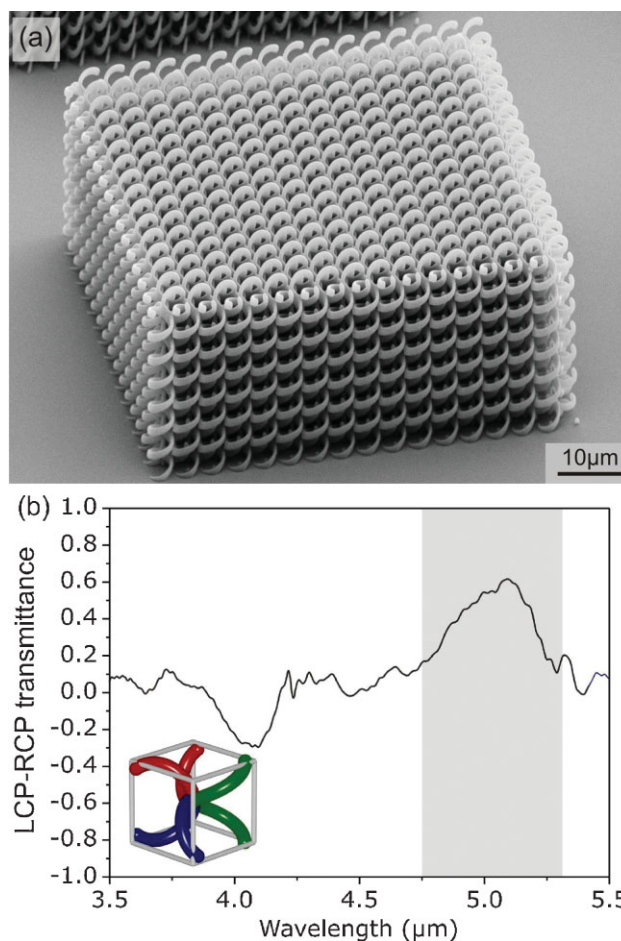


Figure 9. a) SEM image of a right/right bi-chiral photonic crystal. b) Experimental LCP–RCP transmittance data measured at a structure similar to the one shown in a. The inset shows the corresponding unit cell of the structure.

fictitious atoms, one still has to correctly determine the connections between these atoms. For Shechtman's quasicrystals, this is not a problem as binding forces keep the atoms in place. However, for the fabrication of a mechanically stable 3D polymeric structure, this is a crucial aspect. Furthermore, the air voids also need to be connected, as the photoresist cannot be washed out of the underexposed regions otherwise. We address these points starting with a 6D simple-cubic lattice of fictitious points, connected to all of their nearest neighbors by fictitious segments. To achieve an icosahedral quasicrystal structure, this 6D simple-cubic crystal is rotated around the point $(0,0,0,0,0,0)$ by the 6×6 matrix^[46,89] M given by

$$M = \frac{1}{\sqrt{2\tau + 4}} \begin{pmatrix} \tau & \tau & 0 & -1 & 0 & 1 \\ 0 & 0 & 1 & \tau & 1 & \tau \\ 1 & -1 & -\tau & 0 & \tau & 0 \\ \tau & -\tau & 1 & 0 & -1 & 0 \\ -1 & -1 & 0 & -\tau & 0 & \tau \\ 0 & 0 & \tau & -1 & \tau & -1 \end{pmatrix} \quad (1)$$

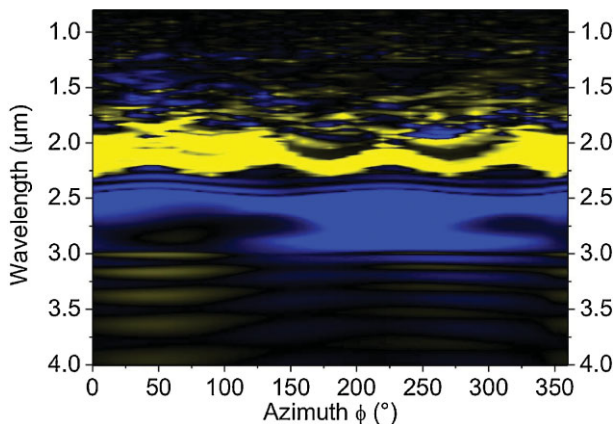


Figure 10. Numerical calculation: angular resolved LCP-RCP transmittance spectra of a silicon right/right bi-chiral photonic crystal. Blue areas correspond to 100% transmittance of LCP light; yellow areas to 100% transmittance of RCP light. Light is impinging with 45° of incidence with respect to the surface normal.

where $\tau = (5^{1/2} + 1)/2$ is the golden mean. The first three coordinates represent the real space position of the atom. Whether an atom is projected at all is decided by the second three coordinates of the resulting 6D vector. If these coordinates fall into the so-called acceptance domain, the real space atom is projected. Selecting atoms with an acceptance domain is necessary, as the projection of all atoms in the 6D space would result in a dense set of atoms in real space. Real space atoms are connected with rods of length l if their counterparts in 6D space are also connected. Along these lines the underlying icosahedral symmetry is not disturbed by the connecting lines. Here, we use $l = 2 \mu\text{m}$, resulting in near-IR photonic quasicrystals.

Proper orientation of the projected 3D quasicrystal allows the inspection of all principal symmetry axes. Figure 11a,e,i show electron microscopy images of a photonic quasicrystal oriented along the local fivefold, threefold, and twofold axes.

To further characterize the symmetry-properties of these quasicrystals Laue diffraction patterns are measured. For this task a solid-state laser at 532-nm wavelength is focused onto the samples by means of a 5-cm focal length lens. The Laue diffraction pattern is scattered off a white sheet of paper and photographed (the overwhelming 0th order diffracted peak is blocked in order not to overload the camera). The three columns of Figure 11 starting with (b), (c), and (d) correspond to Laue diffraction diagrams measured on samples with $4 \mu\text{m}$ and $8 \mu\text{m}$ thickness and a corresponding numerical calculation. Following Ref. 80, these Laue

diagrams are generated by first computing the diffraction pattern of the constituting 6D simple-cubic translational lattice. This diffraction pattern is then projected onto the first three coordinates. This procedure leads to a dense set of diffraction peaks. The intensity of each peak is proportional to $\text{sinc}^2(\pi \Delta k)$, with Δ being the extension of the projected Wigner-Seitz cell and the modulus k of the 3D vector formed by the lower three components of the 6D reciprocal vector. The resulting intensity of a diffraction peak is indicated by the area of the green spot. Spots below an arbitrarily chosen intensity are not shown for clarity.

This procedure obviously leads to good agreement between experiment and theory. Especially, the tenfold symmetry expected for the fivefold axis in real space is nicely obtained. Note, that with an increasing number of lattice planes, the diffraction peaks become sharper. This is obvious from comparing the second and third columns in Figure 11, but can also be observed increasing the number of lattice planes N while going from twofold ($N = 13$) to fivefold ($N = 10$), and finally to threefold ($N = 21$) symmetry (see Fig. 11j,b,f). While the computation of the Laue diagrams is relatively simple and straightforward, the quasi-periodicity prevents a simple approach for calculating transmittance and reflection spectra. As the above scattering-matrix approach is based on structures that are periodic in the xy -plane, the spectral properties of the quasicrystals itself cannot directly be computed along these lines. However, knowledge of so-called “approximants” from previous work on Shechtman’s quasicrystals comes to the rescue.

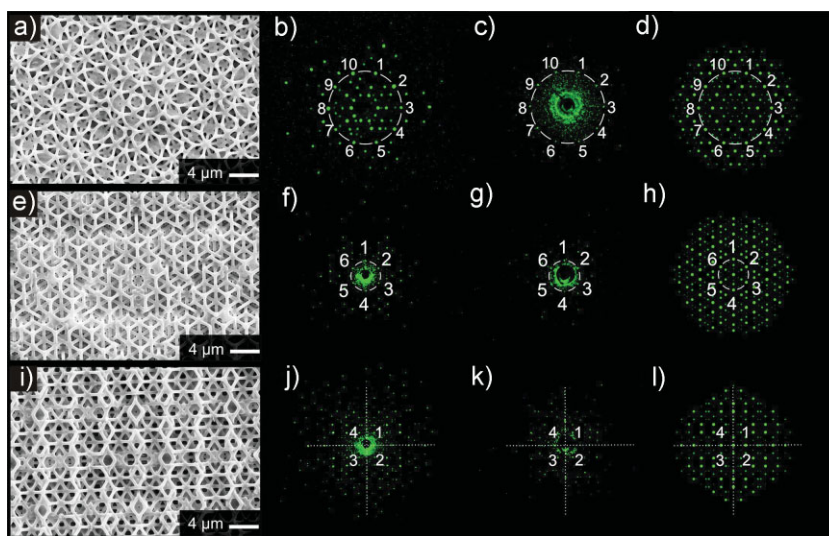


Figure 11. Laue diffraction diagrams of polymeric quasicrystals. a,e,i) Close-up electron microscopy images of icosahedral structures with $l = 2 \mu\text{m}$, $d = 100 \mu\text{m}$, and local fivefold ($N = 15$) (a), threefold ($N = 21$) (e), and twofold ($N = 13$) (i) real-space symmetry. The green spots in columns two and three are the measured Laue diffraction diagrams of 3D quasicrystal templates using a 532 nm laser. b,f,j) Icosahedral structures with $4 \mu\text{m}$ thickness. c,g,k) Corresponding Laue diagrams for samples with $8 \mu\text{m}$ thickness. d,h,l) The green spots are the calculated Laue diffraction diagrams. The sizes and brightnesses of the spots are a measure of the diffraction peak intensity. Reproduced with permission from [46]. Copyright 2006 Nature Publishing Group, Macmillan.

5.1. Approximants

For the construction of rational approximants we employ basically the same mathematical procedure used for the generation of the quasicrystal.^[91] Recall, that we have employed an irrational number τ for the matrix M , which is responsible for the rotation of the structure with respect to the axes of the coordinate system. This irrational number ensures that under the projection a quasiperiodic structure emerges. Rather, choosing a rational number close to τ leads to a periodic structure. The closer the rational number τ comes to the original number, the larger the resulting unit cell size of the approximant becomes in real space. Inside this unit cell, the approximant is strictly identical to the actual quasicrystal. Outside of that unit cell, the approximant only qualitatively resembles the quasicrystal. This aspect is graphically illustrated in Figure 12 for the icosahedral 3D photonic quasicrystal of interest and for a local twofold symmetry axis. From the top to bottom row, Figure 12 also shows the associated 3/2 (Fig. 12c), 2/1 (Fig. 12e), and 1/1 (Fig. 12g) approximants. The unit cell is highlighted in red in each case. These approximants are fabricated just like the quasicrystals, allowing for an experimental decision, regarding which order of approximants is sufficient to model the optical properties of the full quasicrystal.^[91] The right column of Figure 12 shows electron microscopy images of the experimentally realized approximants. Comparison to the left column reveals the high fidelity of the direct laser written structures. Angle-resolved spectroscopy on the approximants as well as on the quasicrystals demonstrates that the 2/1 approximant is already sufficient to describe the optical properties of the full quasicrystal.^[91]

With this approximant approach, we have established a numerical tool to calculate the optical properties of the experimentally realized photonic quasicrystals. Furthermore, this allows us now to tackle the photonic transport properties of the quasicrystals. Experimentally, we measure the transport properties in an upconversion experiment (for details see Ref. 46). Time-resolving the response for incident femtosecond laser pulses reveals a large shift of the transmitted pulse maximum as well as a trailing exponential tail.^[46] Figure 13a shows the experimental data obtained on a quasicrystal oriented along its threefold axis. The dashed curve represents the reference pulse, measured with only the glass substrate and without the sample. Moving the sample into the beam generates a response shown by the solid curve. A single-exponential fit to the tail (solid red line) reveals a decay time of roughly 102 fs. Such exponential tails have previously been observed in disordered systems, where multiple scattering of light on the disordered sites leads to a diffusive transport throughout the structure. Thus, at first sight, one might also expect that small fabrication deficiencies—although not perceivable by eye from the SEM images—might lead to similar behavior in the photonic quasicrystals. This is a valid argument. However, it has been unclear whether or not even a perfect photonic quasicrystal might also deliver such behavior. Using the rational approximants, we are now in a position to directly test this question.

We consider a linearly polarized incident Gaussian optical pulse of 150-fs in duration. For each diffraction order, the square modulus of the Fourier transform of the frequency-dependent transmitted electric field orthogonal to the incident polarization^[46]

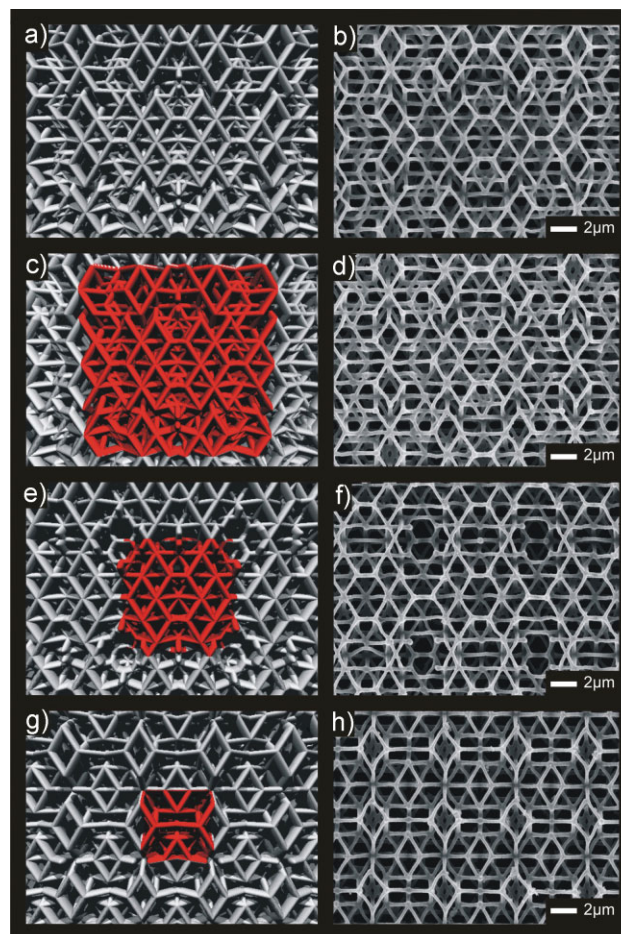


Figure 12. 3D icosahedral photonic quasicrystal and its approximants. The left-hand side column shows computer generated images, the right-hand side column SEM images of corresponding SU-8 structures fabricated via direct laser writing. a,b) The 3D quasicrystal (twofold local axis), c,d) the 3/2 approximant, e,f) the 2/1 approximant, and g,h) the 1/1 approximant. The red-highlighted areas in the left-hand side column mark the unit-cell of the corresponding approximant. Reproduced with permission from [90]. Copyright 2009 Optical Society of America.

delivers the time-resolved intensity. The orthogonal polarization configuration is advantageous as directly transmitted light is suppressed. Hence, we predominantly observe the light that has interacted with the sample. The sum over the various diffracted orders within an opening angle of $\vartheta = 27^\circ$ (corresponding to typical experimental conditions^[46]) is depicted in Figure 13b. In our corresponding scattering-matrix calculations, the rod length is $l = 1 \mu\text{m}$ and the pulse center wavelength is 735 nm. Due to the scalability of Maxwell's equations, the strictly identical result is obtained for 2- μm rod length and 1.47- μm center wavelength, hence corresponding exactly to the parameters used in our experiments.^[46] The numerical results qualitatively reproduce the experimental behavior: the maximum of the transmitted pulse envelope is shifted with respect to time zero and an exponential tail develops. Note, that the approximants used in the calculations are free of any fabrication disorder. The experimentally observed

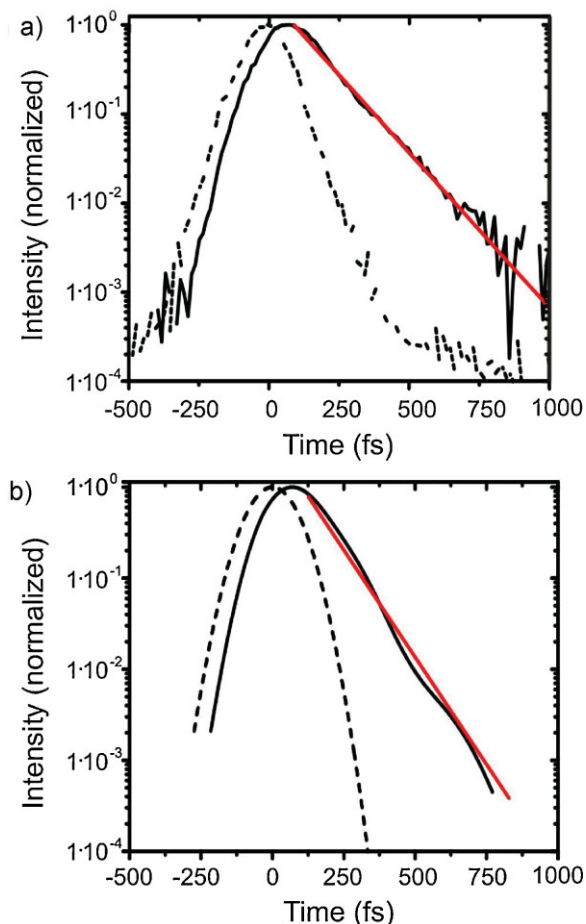


Figure 13. Time-resolved transmittance: a) experimental data (solid) through a quasicrystal oriented along its threefold axis for normal incidence of linear polarized light. The transmitted light is detected in the linear polarization orthogonal to the incident one. b) Calculated transmittance (solid) through a 2/1 approximant of a quasicrystal (see Fig. 12e) for normal incidence of a 150-fs Gaussian optical pulse centered around 735 nm. The emerging light is collected in an opening angle of $\vartheta = 27^\circ$ around the surface normal and in the linear polarization orthogonal to the incident one. The calculated behavior nicely agrees with the experimental one (a). Dashed lines mark the reference without the sample, and solid red curves show the single-exponential fit to the tail (b). Reproduced with permission from [90]. Copyright 2009 Optical Society of America.

behavior is therefore compatible with an intrinsic property of quasicrystals and not necessarily a consequence of low sample quality. Furthermore, experimentally as well as theoretically a strong wavelength dependence of this temporal behavior is found.^[90] A detailed understanding of the underlying transport channels and their dependence on symmetry and wavelength is at the heart of future studies. Introducing functional defects into photonic quasicrystals might be a further step. Here, the very different atomic neighborhoods throughout the quasicrystals will lead to much richer optical properties than known from “normal” photonic crystals. Furthermore, symmetries other than icosahedral symmetries can be studied.

6. Conclusions and Outlook

Over the course of about a decade, direct laser writing has matured from a laboratory curiosity to a reliable and versatile lithography tool allowing for the reliable fabrication of 3D polymer nanostructures down to about 100-nm lateral feature size—even using commercially available instruments (e.g., <http://www.nanoscribe.de>, last accessed February, 2010). Subsequent coating, inversion, or double-inversion of these templates using atomic-layer deposition and/or chemical-vapor deposition allows for converting these structures, e.g., into silicon. Some of the most recent developments in this field are reviewed in this article. This comprises 3D silicon-based near-IR complete photonic bandgap materials, defect cavities therein, uniaxial chiral polymeric photonic crystals, more isotropic bi-chiral helical photonic crystals that might allow for complete polarization stopbands, and near-IR 3D photonic quasicrystals.

Yet, these and related technologies have much more to offer than just dielectric structures. For example, nonlinear or metallic constituent materials can be introduced. Regarding the latter, silver coating of polymer templates by means of chemical-vapor deposition^[91] or gold infilling via electroplating^[51] has led to interesting bi-anisotropic and chiral optical properties of 3D metamaterials, respectively. Furthermore, tailored 3D mechanically flexible structures can serve as novel scaffolds for biological cell culture studies.^[92]

The spatial resolution of direct laser writing as described in this review can be much smaller than the free-space wavelength of the writing laser used. Nevertheless, the minimum feature size is fundamentally limited by the wavelength of light. In contrast, the spatial resolution of stimulated emission depletion (STED) microscopy^[93] is, essentially, diffraction-unlimited. Inspired by this breakthrough in microscopy, Refs. ^[94] and ^[95] have recently demonstrated feature-size reductions with lithography setups using two lasers. Along these lines, minimum feature sizes of some tens of nanometers might come into reach within the next few years.

7. Experimental

Direct Laser Writing: For the direct-laser writing of the structures shown throughout this article, laser light is coupled into an inverted microscope (Leica DM-IRM and Zeiss AxioObserver) and focused into the negative-tone photoresist SU-8 (MicroChem) using a microscope objective with a numerical aperture of 1.4. SU-8 is spincoated onto thin glass cover slips (170 μm thickness) and prebaked following the procedure required by the manufacturer. The sample is mounted onto a three-axis piezo stage (200 $\mu\text{m} \times 200 \mu\text{m} \times 20 \mu\text{m}$ or 300 $\mu\text{m} \times 300 \mu\text{m} \times 300 \mu\text{m}$ travel, Physik Instrumente) and scanned with respect to the focus. For the fabrication of the photonic crystal heterostructure, quasicrystals, and approximants, a regeneratively amplified Ti:Sa laser (120 fs pulse duration at a wavelength of 800 nm, SpectraPhysics Hurricane) is used as the laser source. For the uniaxial spiral structure, the laser source is a Ti:Sa oscillator (100 fs pulse duration at a wavelength of 800 nm). Laser intensity in both setups is controlled with a half-wave plate/polarizer combination and an electromagnetically operated shutter in front of the microscope objective. For the fabrication of the bi-chiral photonic crystals and the photonic-crystal-cavity structures a commercial DLW system is used (PhotonicProfessional, Nanoscribe GmbH), equipped with a frequency-doubled ultrafast fiber-laser (below 150 fs pulse duration at 780 nm wavelength) as laser source.

After exposure the samples are post-baked and developed following the instructions for the usage of SU-8.

Transmittance Spectroscopy: The setups are described in detail in Refs. 40, 44, and 45.

Time-Resolved Upconversion Spectroscopy: The setup is described in Ref. 46.

8. Theoretical

Scattering-Matrix Calculations: In the present article, we have focused on the fabrication and characterization of 3D structures that exhibit 2D periodicity in the lateral xy -plane and are finite in the third direction (z -axis). Experimentally accessible are the values of the transmittance and reflectance, either angularly resolved, e.g., for specific diffraction orders, or angularly integrated, i.e., the total transmittance and reflectance into a half-space. Therefore, corresponding computations for such systems are closely connected to certain problems in the area of diffractive optics where plane waves of given frequency and incoming angle illuminate a rather complex grating structure that is several wavelengths deep and possesses a lateral unit cell with complicated geometries and large index contrast that changes with depth. This implies that the full vectorial nature of the electromagnetic field has to be taken into account and, thus, limits the number of methods that can be applied.

Perhaps the most popular methodology for solving these problems employs a two-stage approach. First, the structure is discretized along the propagation direction in a stair-case fashion ("slicing"); i.e., in each slice the material parameters are assumed to be constant along the z -direction, but their lateral distributions are different from slice to slice. As a result of this approximation, one may—in each slice—decompose the electromagnetic field into a set of eigenmodes. In the lateral plane, these modes are Bloch modes and they exhibit an exponential dependence along the z -axis. These modes and their propagation constants (wave-vector components in z -direction) are determined via a plane-wave expansion that implements that lateral periodicity. This allows determining both types of modes, i.e., those that propagate and those that are evanescent along the z -direction. In particular, it is important to retain, besides all propagating modes, a sufficient number of evanescent modes so that near-field effects can adequately be described.

In a second step, the different expansions of the electromagnetic field in different slices have to be made consistent by enforcing appropriate boundary conditions at the interfaces between slices. As a result, two adjacent slices may be combined to one larger slice. Here, care has to be exerted in order to avoid exponentially growing factors that have their origin in the evanescent modes alluded to above. This is facilitated by one of several possible recursive scattering-matrix algorithms [96] that relate the outgoing modes from a given slice, i.e., the modes that are propagating and evanescently decaying away from the slice, to the corresponding incoming modes onto that slice, i.e., the modes that are propagating and evanescently decaying towards the slice. When all internal interfaces between slices have been eliminated, the total scattering matrix associated with the entire structure is obtained and one may read off the transmittance and reflectance coefficients into the corresponding Bragg orders.

In the diffractive optics community, the approach described above is generally referred to as rigorous coupled wave analysis (RCWA) or Fourier modal method (FMM) [97–100] while in the photonic-crystal community it is more often known as the scattering-matrix approach [101,102]. In this review, we have used the latter terminology throughout.

Finally, we want to note that similar to the case of plane-wave-based photonic band structure calculations, proper Fourier factorization [99,100,103] leads to considerable convergence speed-ups which are of paramount importance when large index contrast or complicated unit cells (such as in supercell calculations) have to be analyzed. When equipped with appropriate absorbing boundary conditions, the scattering-matrix approach can even be extended to nonperiodic systems [104,105].

Acknowledgements

We acknowledge support by the Deutsche Forschungsgemeinschaft (DFG) and the State of Baden-Württemberg through the DFG–Center for Functional Nanostructures (CFN) within subprojects A1.1 and A1.4. The research of G.v.F. is further supported through a DFG Emmy-Noether fellowship (DFG-Fr 1671/4-3). The PhD education of M.T., A.L., I.S., and S.E. is embedded in the Karlsruhe School of Optics & Photonics (KSOP). Some of the computations were performed on the HPXC4000 at Steinbuch Center for Computing (SCC) Karlsruhe under project NOTAMAX. We especially acknowledge the hard work of all undergraduate and graduate students and our collaboration partners: S. John, G. A. Ozin, C. M. Soukoulis, and D. S. Wiersma.

Received: September 29, 2009

Published online: March 18, 2010

- [1] C. Lopez, *Adv. Mater.* **2003**, *15*, 1679.
- [2] P. V. Braun, S. A. Rinne, F. Garcia-Santamaria, *Adv. Mater.* **2006**, *18*, 2665.
- [3] K. Busch, G. von Freymann, S. Linden, S. F. Mingaleev, L. Tkeshelashvili, M. Wegener, *Phys. Rep.* **2007**, *444*, 101.
- [4] D. Norris, E. Arlinghaus, L. Meng, R. Heiny, L. Scriven, *Adv. Mater.* **2004**, *16*, 1393.
- [5] M. Campbell, D. Sharp, M. Harrison, R. Denning, A. Turberfield, *Nature* **2000**, *404*, 53.
- [6] S. Jeon, E. Menard, J. Park, J. Maria, M. Meitl, J. Zaumseil, J. Rogers, *Adv. Mater.* **2004**, *16*, 1369.
- [7] D. Shir, E. C. Nelson, Y. C. Chen, A. Brzezinski, H. Liao, P. V. Braun, P. Wiltzius, K. H. A. Bogart, J. A. Rogers, *Appl. Phys. Lett.* **2009**, *94*.
- [8] A. Blanco, E. Chomski, S. Gratchak, M. Ibsate, S. John, S. W. Leonard, C. Lopez, F. Meseguer, H. Miguez, J. P. Mondia, G. A. Ozin, O. Toader, H. M. van Driel, *Nature* **2000**, *405*, 437.
- [9] A. Arsenault, F. Fleischhaker, G. von Freymann, V. Kitaev, H. Miguez, A. Mihi, N. Tetreault, E. Vekris, I. Manners, S. Aitchison, D. Perovic, G. A. Ozin, *Adv. Mater.* **2006**, *18*, 2779.
- [10] E. Vekris, V. Kitaev, G. von Freymann, D. Perovic, J. Aitchison, G. A. Ozin, *Adv. Mater.* **2005**, *17*, 1269.
- [11] S. A. Rinne, F. Garcia-Santamaria, P. V. Braun, *Nat. Photonics* **2008**, *2*, 52.
- [12] L. Cai, X. Yang, Y. Wang, *Opt. Lett.* **2002**, *27*, 900.
- [13] C. Ullal, M. Maldovan, E. Thomas, G. Chen, Y. Han, S. Yang, *Appl. Phys. Lett.* **2004**, *84*, 5434.
- [14] D. Meisel, M. Wegener, K. Busch, *Phys. Rev. B* **2004**, *70*, 165104.
- [15] T. Chan, O. Toader, S. John, *Phys. Rev. E* **2005**, *71*, 046605.
- [16] Y. Miklyayev, D. Meisel, A. Blanco, G. von Freymann, K. Busch, W. Koch, C. Enkrich, M. Deubel, M. Wegener, *Appl. Phys. Lett.* **2003**, *82*, 1284.
- [17] W.-D. Mao, G.-Q. Liang, Y.-Y. Pu, H.-Z. Wang, Z. Zeng, *Appl. Phys. Lett.* **2007**, *91*, 261911.
- [18] D. Xu, K. P. Chen, A. Harb, D. Rodriguez, K. Lozano, Y. Lin, *Appl. Phys. Lett.* **2009**, *94*, 231116.
- [19] T. Chan, O. Toader, S. John, *Phys. Rev. E* **2006**, *73*, 046610.
- [20] T. Y. M. Chan, S. John, *Phys. Rev. A* **2008**, *78*, 033812.
- [21] M. Hermatschweiler, A. Ledermann, G. A. Ozin, M. Wegener, G. von Freymann, *Adv. Funct. Mater.* **2007**, *17*, 2273.
- [22] F. Garcia-Santamaria, M. Xu, V. Lousse, S. Fan, P. V. Braun, J. A. Lewis, *Adv. Mater.* **2007**, *19*, 1567.
- [23] N. Tetreault, G. von Freymann, M. Deubel, M. Hermatschweiler, F. Pérez-Willard, S. John, M. Wegener, G. A. Ozin, *Adv. Mater.* **2006**, *18*, 457.
- [24] G. Gratson, F. Garcia-Santamaria, V. Lousse, M. Xu, S. Fan, J. Lewis, P. Braun, *Adv. Mater.* **2006**, *18*, 461.
- [25] J. S. King, E. Graugnard, O. M. Roche, D. N. Sharp, J. Scringeout, R. G. Denning, A. J. Turberfield, C. J. Summers, *Adv. Mater.* **2006**, *18*, 1561.
- [26] J. H. Moon, Y. Xu, Y. Dan, S.-M. Yang, A. T. Johnson, S. Yang, *Adv. Mater.* **2007**, *19*, 1510.

- [27] J. H. Moon, S. Yang, W. Dong, J. W. Perry, A. Adibi, S.-M. Yang, *Opt. Express* **2006**, *14*, 6297.
- [28] N. Yamamoto, S. Noda, A. Chutinan, *Jpn. J. Appl. Phys. Part 2* **1998**, *37*, L1052.
- [29] S. Lin, J. Fleming, D. Hetherington, B. Smith, R. Biswas, K. Ho, M. Sigalas, W. Zubrzycki, S. Kurtz, J. Bur, *Nature* **1998**, *394*, 251.
- [30] S. Noda, K. Tomoda, N. Yamamoto, A. Chutinan, *Science* **2000**, *289*, 604.
- [31] M. H. Qi, E. Lidorikis, P. T. Rakich, S. G. Johnson, J. D. Joannopoulos, E. P. Ippen, H. I. Smith, *Nature* **2004**, *429*, 538.
- [32] A. Tandraechanurat, S. Ishida, K. Aoki, D. Guimand, M. Nomura, S. Iwamoto, Y. Arakawa, *Appl. Phys. Lett.* **2009**, *94*, 171115.
- [33] J. Smay, J. Cesarano, J. Lewis, *Langmuir* **2002**, *18*, 5429.
- [34] C. N. LaFratta, J. T. Fourkas, T. Baldacchini, R. A. Farrer, *Angew. Chem. Int. Ed.* **2007**, *46*, 6238.
- [35] S. Maruo, J. T. Fourkas, *Laser Photonics Rev.* **2008**, *2*, 100.
- [36] S. Ogawa, M. Imada, S. Yoshimoto, M. Okano, S. Noda, *Science* **2004**, *305*, 227.
- [37] H.-B. Sun, S. Matsuo, H. Misawa, *Appl. Phys. Lett.* **1999**, *74*, 786.
- [38] S. Kawata, H.-B. Sun, T. Tanaka, K. Takada, *Nature* **2001**, *412*, 697.
- [39] M. Straub, M. Gu, *Opt. Lett.* **2002**, *27*, 1824.
- [40] M. Deubel, G. von Freymann, M. Wegener, S. Pereira, K. Busch, C. Soukoulis, *Nat. Mater.* **2004**, *3*, 444.
- [41] M. Deubel, M. Wegener, A. Kaso, S. John, *Appl. Phys. Lett.* **2004**, *85*, 1895.
- [42] K. K. Seet, V. Mizeikis, K. Kannari, S. Juodkazis, H. Misawa, N. Tetreault, S. John, *IEEE J. Sel. Top. Quantum Electron.* **2008**, *14*, 1064.
- [43] K. K. Seet, V. Mizeikis, S. Matsuo, S. Juodkazis, H. Misawa, *Adv. Mater.* **2005**, *17*, 541.
- [44] M. Thiel, M. Decker, M. Deubel, M. Wegener, S. Linden, G. von Freymann, *Adv. Mater.* **2007**, *19*, 207.
- [45] M. Thiel, M. S. Rill, G. von Freymann, M. Wegener, *Adv. Mater.* **2009**, *21*, 4680.
- [46] A. Ledermann, L. Cademartiri, M. Hermatschweiler, C. Toninelli, G. A. Ozin, D. S. Wiersma, M. Wegener, G. von Freymann, *Nat. Mater.* **2006**, *5*, 942.
- [47] S. Wong, M. Deubel, F. Perez-Willard, S. John, G. A. Ozin, M. Wegener, G. von Freymann, *Adv. Mater.* **2006**, *18*, 265.
- [48] S. H. Wong, M. Thiel, P. Brodersen, D. Fenske, G. A. Ozin, M. Wegener, G. von Freymann, *Chem. Mater.* **2007**, *19*, 4213.
- [49] S. Wong, O. Kiowski, M. Kappes, J. K. N. Lindner, N. Mandal, F. C. Peiris, G. A. Ozin, M. Thiel, M. Braun, M. Wegener, G. von Freymann, *Adv. Mater.* **2008**, *20*, 4097.
- [50] Y.-S. Chen, A. Tal, D. B. Torrance, S. M. Kuebler, *Adv. Funct. Mater.* **2006**, *16*, 1739.
- [51] J. K. Gansel, M. Thiel, M. S. Rill, M. Decker, K. Bade, V. Saile, G. von Freymann, S. Linden, M. Wegener, *Science* **2009**, *325*, 1513.
- [52] A. Chutinan, S. John, *Phys. Rev. E* **2005**, *71*, 026605.
- [53] D. C. Meisel, M. Diem, M. Deubel, F. Perez-Willard, S. Linden, D. Gerthsen, K. Busch, M. Wegener, *Adv. Mater.* **2006**, *18*, 2964.
- [54] A. Ovsianikov, X. Shizhou, M. Farsari, M. Vamvakaki, C. Fotakis, B. N. Chichkov, *Opt. Express* **2009**, *17*, 2143.
- [55] M. Deubel, M. Wegener, S. Linden, G. von Freymann, *Appl. Phys. Lett.* **2005**, *87*, 221104.
- [56] E. Istrate, M. Charbonneau-Lefort, E. H. Sargent, *Phys. Rev. B* **2002**, *66*, 075121.
- [57] A. Chutinan, S. John, *Phys. Rev. Lett.* **2003**, *90*, 123901.
- [58] A. Chutinan, S. John, *Photonics Nanostruct.* **2004**, *2*, 41.
- [59] A. Chutinan, S. John, *Opt. Expr.* **2006**, *14*, 1266.
- [60] M. Deubel, M. Wegener, S. Linden, G. von Freymann, S. John, *Opt. Lett.* **2006**, *31*, 805.
- [61] K. Busch, S. Mingaleev, M. Schillinger, D. Hermann, *J. Phys.: Condens. Matter* **2003**, *15*, R1233.
- [62] D. Hermann, M. Schillinger, S. F. Mingaleev, K. Busch, *J. Opt. Soc. Am. B* **2008**, *25*, 202.
- [63] a) A. Chutinan, S. Noda, *Phys. Rev. B* **1998**, *57*, 2006. b) O. Toader, S. John, *Science* **2001**, *292*, 1133.
- [64] S. R. Kennedy, M. J. Brett, O. Toader, S. John, *Nano Lett.* **2002**, *2*, 59.
- [65] P. C. P. Hruudey, B. Szeto, M. J. Brett, *Appl. Phys. Lett.* **2006**, *88*, 251106.
- [66] Y. K. Pang, J. C. W. Lee, H. F. Lee, W. Y. Tam, C. T. Chan, P. Sheng, *Opt. Exp.* **2005**, *13*, 7615.
- [67] K. K. Seet, V. Mizeikis, S. Juodkazis, H. Misawa, *Appl. Phys. A* **2006**, *82*, 683.
- [68] J. Lee, C. Chan, *Opt. Exp.* **2005**, *13*, 8083.
- [69] S. Furumi, Y. Sakka, *Adv. Mater.* **2006**, *18*, 775.
- [70] M. Mitov, N. Dessaud, *Nat. Mater.* **2006**, *5*, 361.
- [71] J. Hwang, M. H. Song, B. Park, S. Nishimura, T. Toyooka, J. W. Wu, Y. Takahashi, K. Ishikawa, H. Takezoe, *Nat. Mater.* **2005**, *4*, 383.
- [72] M. Thiel, G. von Freymann, M. Wegener, *Opt. Lett.* **2007**, *32*, 2547.
- [73] W. Cao, A. Muñoz, P. Palffy-Muhoray, B. Taheri, *Nat. Mater.* **2002**, *1*, 111.
- [74] H. Kikuchi, M. Yokota, Y. Hisakado, H. Yang, T. Kajiyama, *Nat. Mater.* **2002**, *1*, 64.
- [75] H. J. Coles, M. N. Pivnenko, *Nature* **2005**, *436*, 997.
- [76] S. Meiboom, J. P. Sethna, P. W. Anderson, W. F. Brinkman, *Phys. Rev. Lett.* **1981**, *46*, 1216.
- [77] D. Shechtman, I. Blech, D. Gratias, J. W. Cahn, *Phys. Rev. Lett.* **1984**, *53*, 1951.
- [78] D. Levine, T. C. Lubensky, S. Ostlund, S. Ramaswamy, P. J. Steinhardt, J. Toner, *Phys. Rev. Lett.* **1985**, *54*, 1520.
- [79] P. J. Steinhardt, S. Ostlund, *The Physics of Quasicrystals*, World Scientific, Singapore **1987**.
- [80] C. Janot, *Quasicrystals*, Clarendon Press, Oxford **1992**.
- [81] L. Bindi, P. J. Steinhardt, N. Yao, P. J. Lu, *Science* **2009**, *324*, 1306.
- [82] M. E. Zoorob, M. D. B. Charlton, G. J. Parker, J. J. Baumberg, M. C. Nett, *Nature* **2000**, *404*, 740.
- [83] B. Freedman, G. Bartal, M. Segev, R. Lifshitz, D. N. Christodoulides, J. W. Fleischer, *Nature* **2006**, *440*, 1166.
- [84] W. Steurer, D. Sutter-Widmer, *J. Phys. D* **2007**, *40*, R229.
- [85] Y. Roichman, D. G. Grier, *Opt. Express* **2005**, *13*, 5434.
- [86] Y. Yang, G. P. Wang, *Appl. Phys. Lett.* **2006**, *89*, 111104.
- [87] I. Bitá, T. Choi, M. E. Walsh, H. L. Smith, E. L. Thomas, *Adv. Mater.* **2007**, *19*, 1403.
- [88] D. Shir, H. Liao, S. Jeon, D. Xiao, H. T. Johnson, G. R. Bogart, K. H. A. Bogart, J. A. Rogers, *Nano Lett.* **2008**, *8*, 2236.
- [89] F. H. Li, L. C. Wang, *J. Phys. C: Solid State Phys.* **1988**, *21*, 495.
- [90] A. Ledermann, D. S. Wiersma, M. Wegener, G. von Freymann, *Opt. Expr.* **2009**, *17*, 1844.
- [91] M. S. Rill, C. Plet, M. Thiel, I. Staude, G. von Freymann, S. Linden, M. Wegener, *Nat. Mater.* **2008**, *7*, 543.
- [92] F. Klein, T. Striebel, J. Fischer, Z. Jiang, C. Franz, G. von Freymann, M. Wegener, M. Bastmeyer, *Adv. Mater.* **2009**, in press, DOI: 10.1002/adma.200902515.
- [93] T. A. Klar, S. Jakobs, M. Dyba, A. Egner, S. W. Hell, *Proc. Natl. Acad. Sci. USA* **2000**, *97*, 8206.
- [94] L. Li, R. R. Gattass, E. Gershgoren, H. Hwang, J. T. Fourkas, *Science* **2009**, *324*, 910.
- [95] T. F. Scott, B. A. Kowalski, A. C. Sullivan, C. N. Bowman, R. R. McLeod, *Science* **2009**, *324*, 913.
- [96] L. Li, *J. Opt. Soc. Am. A* **1996**, *13*, 1024.
- [97] M. G. Moharam, E. B. Grann, D. A. Pommert, T. K. Gaylord, *J. Opt. Soc. Am. A* **1995**, *12*, 1068.
- [98] G. Granet, B. Guizal, *J. Opt. Soc. Am. A* **1996**, *13*, 1019.
- [99] P. Lalanne, G. M. Morris, *J. Opt. Soc. Am. A* **1996**, *13*, 779.
- [100] L. Li, *J. Opt. Soc. Am. A* **1997**, *14*, 2758.
- [101] D. M. Whittaker, I. S. Culshaw, *Phys. Rev. B* **1999**, *60*, 2610.
- [102] S. G. Tikhodeev, A. L. Yablonskii, E. A. Muljarov, N. A. Gippus, T. Ishihara, *Phys. Rev. B* **2002**, *66*, 045102.
- [103] L. Li, *J. Opt. Soc. Am. A* **1996**, *13*, 1870.
- [104] P. Lalanne, E. Silberstein, *Opt. Lett.* **2000**, *25*, 1092.
- [105] J. P. Hugonin, P. Lalanne, *J. Opt. Soc. Am. A* **2002**, *22*, 1844.